IEEE Access
Multidisciplinary | Rapid Review | Open Access Journal

Received May 3, 2020, accepted May 28, 2020, date of publication June 8, 2020, date of current version June 18, 2020.

Digital Object Identifier 10.1109/ACCESS.2020.3000675

A Ka-Band Receiver Front-End With Noise Injection Calibration Circuit for CubeSats Inter-Satellite Links

FEDERICO ALIMENTI[1], (Senior Member, IEEE), PAOLO MEZZANOTTE[1], (Member, IEEE), GUENDALINA SIMONCINI[1], (Graduate Student Member, IEEE), VALENTINA PALAZZI[1], (Member, IEEE), RAFFAELE SALVATI[1], GIORDANO CICIONI[1], LUCA ROSELLI[1], (Fellow, IEEE), FEDERICO DOGO[2], SIMONE PAULETTO[2], MARIO FRAGIACOMO[2], AND ANNA GREGORIO[2,3]

[1]Department of Engineering, University of Perugia, 06125 Perugia, Italy
[2]PicoSaTs s.r.l., 34127 Trieste, Italy
[3]Department of Physics, University of Trieste, 34149 Trieste, Italy

Corresponding author: Federico Alimenti (federico.alimenti@unipg.it)

ABSTRACT This paper proposes a Ka-band receiver front-end for future CubeSats Low-Earth Orbit (LEO) to Geostationary (GEO) inter-satellite links. The receiver is able to support very high data rates (up to 100 Mbit/s) in Quadrature Phase-Shift Keying (QPSK) when in the line of sight of a GEO satellite that is equipped with a steerable 70-cm antenna and transmitting a 25-W signal. The originality of the proposed approach is twofold. First we will demonstrate the receiver feasibility based on a class of miniaturized and low-cost microwave integrated circuits, currently available on the market. In particular, our receiver is based on a novel combination of integrated Low-Noise Amplifiers (LNA) with an image rejection filter, the latter exploiting the Substrate Integrated Waveguide (SIW) technology. An optimization of the via placement proved to be able to reduce the need for shielding apparatuses, thus simplifying the mechanics and reducing mass, volume and hardware costs. Secondly, we will propose a noise injection circuit capable of measuring and calibrating the receiver gain, also during in-orbit operation. Self testing capabilities are particularly relevant for CubeSats because the usage of commercial components poses serious reliability issues.

INDEX TERMS Ka-band, microwave receivers, noise injection, noise calibration, CubeSats, LEO to GEO links, microwave/mm-wave electronics.

I. INTRODUCTION

In these years satellite launches have been increased, due to easier access to space and to the development of cheaper hardware. Small satellites on Low-Earth Orbit (LEO) play a central role in Earth observation. The improved resolution of their instruments generates high data volumes [1], [2], which can be available in near real time. For this reason, the space community is planning to exploit the existing infrastructure to facilitate the communication between Earth and small LEO satellites. The Fixed Satellite Service (FSS) networks on Geostationary relay satellites, also known as Geosynchronous Equatorial Orbit (GEO) satellites, offer an attractive perspective for providing the required connectivity.

The associate editor coordinating the review of this manuscript and approving it for publication was Yingsong Li.

Data relay in satellite communications is a well-known concept, which has been studied or implemented in different systems, such as the NASA third generation Tracking and Data Relay Satellite System (TDRSS-K), launched in January 2013, and the Japan Aerospace Exploration Agency (JAXA) experimental Data Relay Page Satellite (DRTS), launched in 2002. These systems provide high-rate data relay capabilities mainly between geostationary satellites and the Ground Stations (GS).

The communication link between LEO and Earth is a very well studied subject. Although it can operate with limited link budgets, it requires efficient communication protocols, to overcome the high Doppler effect. Moreover, due to the low orbit, LEO communications suffer from restricted visibility time from the ground station. If a GEO satellite is used as a relay station between the LEO and the ground station, then it

is theoretically possible to increase the contact time to more than half of the LEO orbit. As a consequence, Inter-Satellite Links (ISL) between LEO and GEO are currently under study to provide high-data rates and wide coverage, particularly for the emerging CubeSat market [3].

This work presents a receiver in the Ka-band that supports high-speed links between LEO and GEO satellites [4], [5]. The proposed low noise front-end performs a down conversion of the incoming 29 GHz signal into a 3.7 GHz Intermediate Frequency (IF). The originality of the proposed approach lies in the adoption of a Substrate Integrated Waveguide (SIW) image rejection filter in conjunction with integrated Low-Noise Amplifier (LNA) stages. An optimization of the via layout reduces the need for shielding apparatuses, thus simplifying the mechanics and reducing mass, volume and hardware costs. In last years, many studies related to filters [6], mixers [7]–[9], oscillators [10], [11], low-noise [12]–[15] and power amplifiers [16]–[20] in SIW technology were published. The application of this technology to front-ends, however, is scarcely documented. Active front-ends were discussed in [21]–[23], whereas passive structures are treated in [24]–[26]. In all these papers, however, parameters like gain, stability factor and noise figure were never reported, leaving the field of active front-ends still widely unexplored.

The active front-end reported in the present paper uses a SIW filter between the two LNA stages. This configuration has been selected since it constitutes the best compromise among noise figure, image rejection and input compression point. Furthermore, the ground via external to the SIW filters have been carefully placed with the purpose to minimize the parasitic output-to-input coupling, and thus to achieve the unconditional stability (no LNA self-oscillations). As a result, the LNA reaches a gain of 38 dB without mechanical shields.

As a further original development, the receiver includes a gain calibration circuit based on noise injection at the receiver input. This self-test capability is particularly important in low-cost electronics, such as that exploited in CubeSats. To achieve maximum flexibility, a Software Defined Radio (SDR) is planned for the I/Q demodulation and for the Analog to Digital Conversion (ADC). The decoding operations and the data interface will be carried out by a processor based on Field Programmable Gate Array (FPGA) circuits [27].

To experimentally verify the above concepts, a preliminary front-end breadboard is implemented, operating between 27.5 and 30 GHz. The breadboard, that uses Components Off The Shelf (COTS) and custom developed Printed Circuit Boards (PCB), is characterized by an overall 80 dB gain, a 2.8 dB noise figure and a −37 dBm input-referred 1 dB compression point. The importance of these results is that they have been obtained exploiting a class of miniaturized and low-cost microwave integrated circuits currently available on the market, opening the way to a dense communication infrastructure for CubeSat LEO to GEO inter-satellite links. This infrastructure could be used for commercial applications and for future exploration missions [28], [29].

In summary the original elements of the present paper are:

- development of a novel Ka-band receiver front-end based on the SIW technology with the purpose to avoid shielding elements, simplify the mechanics and reducing mass, volume and hardware costs, patent [30];
- modeling of the spurious coupling mechanisms due to parasitic waveguides and via spacing in the PCB and study of their impact on the LNA stability;
- analysis of the in-orbit receiver gain self test sub-system: for the first time an avalanche noise diode circuit model is combined with the 2-ports scattering matrix of an attenuator to simulate the whole sub-system performance (not just that of the noise diode alone).

II. MISSION SCENARIO

One of the main advantages of the GEO to LEO inter-satellite links is that the radio path is not affected by the atmospheric attenuation that can be as high as 20 dB in heavy rain conditions for services in the Ka-band. As a consequence, very stable and reliable communications can be achieved irrespective of the ground weather.

To guarantee the link, however, both the antennas should be steerable. Although the discussion of this important point is outside the scope of the present paper we can observe that: i) the GEO satellite sees the Earth within a cone of about $\pm 10°$, so the steering angle needed by the GEO antenna to communicate with the LEO satellite are limited [31]; ii) the LEO satellite needs to change the antenna orientation with a velocity of about 4° per minute, being the average orbital period of 90 minutes. Therefore, the antenna requirements are not particularly severe. Mechanically or electronically steerable antennas can be used to this purpose, the most relevant being motorized dish reflectors, active reflectarrays and phased arrays.

Fig. 1 shows a simplified link geometry where the receiver is on the CubeSat in low-earth orbit, exactly at the zenith of a geostationary satellite (GEO). In this figure G_a^{GEO} and G_a^{LEO} are the gains of the GEO and LEO satellite antennas respectively, P_{tx} is the power transmitted by the GEO satellite, and $R = 34986$ km is the minimum LEO to GEO distance. The received power, P_{rx}, is determined using the Friis' formula, assuming a 25 W transmitter onboard the GEO and accounting for 1 dB insertion loss due to the output harmonic suppression filter and to the circulator [31]. The computations have been done at 28.75 GHz, i.e. at the center of the operating frequency band that spans from 27.5 to 30 GHz, see Tab. 1. A dish antenna of 70-cm diameter is considered for the GEO satellite. The LEO CubeSat is equipped with a deployable dish antenna, similar to that described in [29]. Two different diameters have been assumed, namely 40- and 20-cm. This is to study a trade-off between mass/size and received signal strength. The half power beam width of the LEO antenna, θ_H^{LEO}, is equal to about 2° and 4° for the 40- and a 20-cm diameter respectively. In all the cases (GEO, LEO of different diameters) the dish antenna efficiency is assumed to be 60%.

TABLE 1. Ka-band GEO to LEO link budget for 25 W transmitted power.

f_0 (GHz)	G_a^{GEO} (dBi)	EIRP (dBm)	path loss (dB)	D_{rx} (cm)	G_a^{LEO} (dBi)	P_{rx} (dBm)
28.75	44.3	87.3	212.5	40	39.4	-85.8
28.75	44.3	87.3	212.5	20	33.4	-91.7

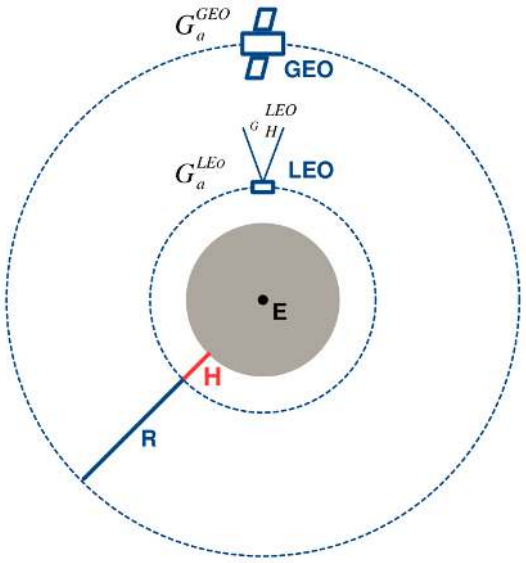

FIGURE 1. Mission scenario used to estimate the maximum received power in downlink (from GEO to LEO). Link parameters: range $R = 34986$ km (minimum LEO to GEO distance); height of the LEO orbit $H = 800$ km; GEO transmitted power $P_{tx} = 25$ W; GEO antenna gain $G_a^{GEO} = 44.3$ dBi (70 cm steerable dish antenna with a 60% efficiency); LEO antenna gain $G_a^{LEO} = 39.4$ dBi (40 cm steerable dish antenna with a 60% efficiency).

The best case receiver noise floor can be estimated assuming a 4 dB receiver noise figure, a 50 MHz signal bandwidth and an antenna noise temperature close to 110 K. Indeed the receiver antenna points toward the cold space (3 K cosmic microwave background) and the antenna noise temperature is dominated by the antenna efficiency and its physical temperature (estimated at 273 K). The input spectral noise density corresponding to 110 K is −171 dBm/Hz and, as a consequence, the receiver noise floor is −94 dBm. With the received power reported in Tab. 1, we get a carrier-to-noise ratio (C/N) of 8.2 and 2.3 dB respectively for the 40- and 20-cm diameters. According to the Shannon-Hartley theorem, the theoretical channel capacity is equal to about 146 and 72 Mbit/s for the two diameters.

III. RECEIVER ARCHITECTURE

The receiver (see top panel of Fig. 2) is based on two subsystems: i) the Ka-band front-end; ii) the Software Defined Radio (SDR) and Field-Programmed Gate Array (FPGA) modem assembly. The Ka-band front-end operates a first down conversion to an Intermediate Frequency (IF) of 3.7 GHz. It consists of a two-stage Low Noise Amplifier (the A1 and A2 LNAs in the figure), an image rejection filter (F1), a Sub-Harmonically pumped (×2) Mixer (SHM), an IF filter

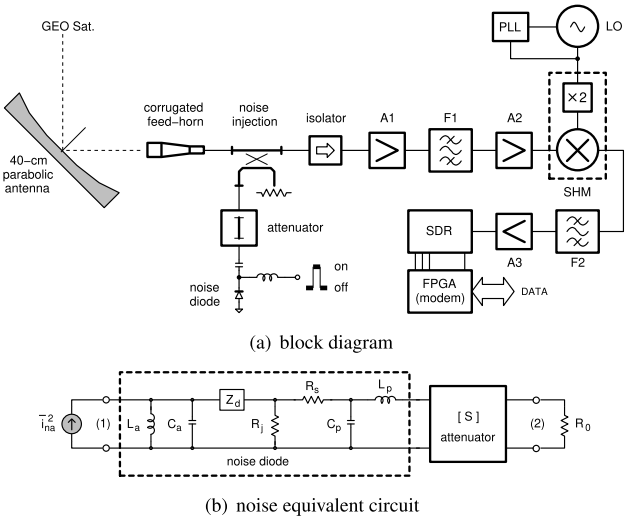

FIGURE 2. Receiver architecture with noise injection circuitry (a) and equivalent circuit for the Excess Noise Ratio (ENR) computation (b). In the receiver, A1 and A2 are the Ka-band LNAs, F1 is the image rejection filter, SHM is the Sub-Harmonic Mixer, F2 is the 3.7 GHz IF filter, A3 is the IF amplifier and SDR is the 6-GHz Software Defined Radio. The NC406 noise diode parameters are reported in [32], whereas the HMC655 attenuator (6 dB up to 50 GHz) from Analog Devices is used to set the ENR value of the designed noise source.

(F2) and a first stage of IF amplification (A3). The half frequency LO is generated by a microwave Phased Locked Loop (PLL) synthesizer, to ensure a low near-carrier phase noise as well as frequency stability and agile channel selection. In the Ka-band, the Local Oscillator (LO) frequency varies from 11.90 to 13.15 GHz. The input isolator (optional) is used to provide a good antenna matching over the operating frequency range. A typical 1-dB insertion loss was already considered in the system analysis by setting the overall noise figure to 4 dB. A 6-GHz SDR and an FPGA-based demodulator (not discussed here) realize the digital baseband section of the high performance DVB-S2 compliant modem. In the following the main issues related to the receiver design are as follows. First of all the gain calibration circuitry is accurately analyzed. Secondly, some aspects of the LNA design (A1, F1, A2 in Fig. 2) will be discussed. In particular the attention is focused on the parasitic output-to-input coupling and to the overall circuit stability. This will be ensured by a proper placing of ground vias in the region outside the SIW image rejection filter.

IV. GAIN CALIBRATION CIRCUITRY DESIGN

An original feature of the receiver front-end is the possibility to be tested and, eventually, calibrated also during in-orbit operation. To this purpose a noise injection circuit is adopted, as shown in Fig. 2 (top panel). Such a circuit is composed by an avalanche noise diode, a bias-tee, an attenuator and a directional coupler. The noise source is controlled by the receiver Central Process Unit (CPU). When the diode is biased into avalanche (high temperature state), a known amount of noise power is injected into the receiver and the corresponding output power, N_{on}, is measured. The latter measurement can

be implemented in several ways, i.e. by exploiting a zero-bias Schottky diode detector at IF output or by using the Received Signal Strength Indication (RSSI) signal provided by the SDR. Similarly, an output power N_{off} is obtained when the noise source is switched off (low temperature state). According to the Y-factor method, the overall receiver gain G_{rx} is given by:

$$G_{rx} = \frac{N_{on} - N_{off}}{k_B\, C\, \mathrm{ENR}\, T_0\, B} \tag{1}$$

where k_B is the Boltzmann constant, C is the coupling factor of the directional coupler, ENR is the Excess Noise Ratio of the avalanche noise source, $T_0 = 290\,\mathrm{K}$ is the IEEE standard temperature and B is the bandwidth of the receiver stages before the power detector. The main advantage of the described procedure is that the gain is determined employing the avalanche noise source only. The described measurement should be carried-out when no signal is received from the GEO satellite.

To measure the receiver noise figure in a laboratory environment, the noise injection must be performed with the receiver terminated on a matched load having a known (physical) temperature. During in-orbit operation, instead, the receiver antenna can be pointed toward a celestial body like the Moon, for example, which behaves as a black-body with a brightness temperature between 260 and 280 K in the Ka-band, [33].

To avoid the receiver saturation during the noise injection phase, the calibration circuit is designed assuming a noise temperature increase $T_i = C\,\mathrm{ENR}\,T_0$ of the same order of magnitude of the antenna noise temperature. Since in [34] it is shown that the NC406 avalanche diode has a 29 dB ENR at 30 GHz (24 mA bias), $T_i \approx 2\,T_0$ implies a 6 dB attenuator and a $C = -20\,\mathrm{dB}$ directional coupler. In order to simulate the ENR behavior versus the frequency, the approach proposed in [35] is applied. The equivalent circuit shown in Fig. 2 is used for the computation, where the attenuator is cascaded to the small-signal model of the avalanche diode, and the ENR is derived from the noise power dissipated on R_0. The graph of Fig. 3 is obtained modeling the 6 dB HMC655 attenuator by means of its measured scattering matrix, this being available from the Analog Devices web site.

From this study it emerges that the ENR in the considered Ka-band decreases from 23.4 dB (at 27.5 GHz) to 22.2 dB (at 30 GHz). To the best of the authors' knowledge, this is the first time that a complete noise source, composed by a diode and an attenuator, is simulated with a CAD software. The same approach could be extended to consider other effects such as the bias-tee, the wire-bonding inductance (for die devices) or package parasitics [36] and the directional coupler frequency response. Although not considered in the present study, we noticed that a flat 24.8 dB ENR can be obtained in the K-band at 22.85 GHz with the same approach. This is another band of potential interest for LEO to GEO inter-satellite links.

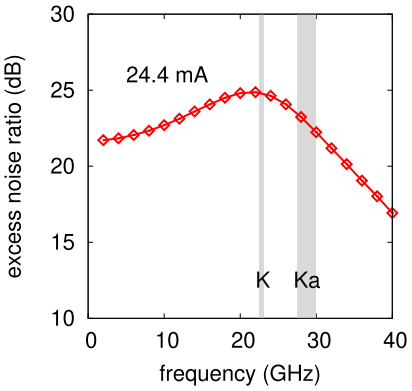

FIGURE 3. Simulated ENR versus frequency. The noise source is composed by the NC406 diode (produced by NoiseCom) connected in cascade with the HMC655 6 dB attenuator (from Analog Devices). The output noise power is computed on $R_0 = 50\,\Omega$.

As a final remark we noticed that, for missions of short duration (a few years) like those of Cubesats, the ENR variation due to the noise source aging can be neglected.

V. LNA DESIGN

The LNA board is designed having in mind two main goals, namely: i) to achieve a certain degree of interferences robustness without compromising the noise figure (a transmitter for the LEO to GEO uplink could be located between 17.8 and 20.2 GHz) and ii) to guarantee an unconditionally-stable operation of the LNA, even without shields and cavities, to reduce mass and costs of the final board.

Functional to these goals is the adoption of the SIW technology for the image rejection filter implementation (see Sec. VI), an approach that leads to intrinsically self-shielded components. The filter is placed between the two gain stages in order to improve the interference robustness, as the signal that leaks-out of the transmitter is strongly rejected by the filter before entering the second stage. Furthermore, since the filter follows a first gain stage, its losses have a negligible effect on the overall noise figure.

Secondly, the interstage filter arrangement allows us to put space between the two gain blocks, significantly reducing the parasitic coupling between the output port of the second stage and the input port of the first one. Placing a sufficient distance between the two stages, however, is not sufficient by itself to avoid parasitic oscillations. Other techniques have been adopted, namely: i) low-radiation transmission lines to feed the LNA; ii) ground vias outside the SIW filter to reduce the parasitic coupling due to waveguide modes between top and bottom ground planes; iii) the extension of the top ground plane reduced to a minimum (compatible with the layout constraints). In the following subsections we will discuss the effectiveness of these approaches using simplified models.

A. PARASITIC C-SHAPED WAVEGUIDES

As stated before, the LNA exploits low-radiation transmission lines like grounded Co-Planar Waveguides (CPW) and

SIW rectangular waveguides. All these lines require a bottom and a top ground plane. Although it is common practice to extend the top ground plane to all the PCB, this approach can cause problems if an adequate number of ground vias is not used. Top and bottom metal planes, indeed, form guiding structures that are able to couple the signal leaking out of the amplifier output back to the input. A parasitic feedback loop is thus formed as in Fig. 4(a), while an approximate model of such a guiding structure is represented by the c-shaped waveguide shown in Fig. 4(b). The cross-section is similar to half of a dielectric-filled rectangular waveguide with one of the two vertical walls constituted by the ground via row, while the other is an open (i.e. radiating) boundary. At this point it is possible to note that, for small substrate thickness h, the open boundary can be approximated with a magnetic wall. Although crude, such an approach reduces the complexity of the problem, and allows us to obtain simple expression of the cutoff frequency f_c as a function of the top metal extension w:

$$f_c \approx \frac{c_0}{4\,w\,\sqrt{\epsilon_R}} \tag{2}$$

where c_0 is the light velocity in a vacuum and ϵ_R is the relative permittivity of the dielectric substrate.

Fig. 4(c) shows the behavior of f_c when w varies in the range from 1 to 7 mm. A dielectric with $\epsilon_R = 3.66$ is considered. The theory (black curve) agrees within ±3% with the CST electromagnetic simulations (points), so eqn. (2) can be used to reliably evaluate f_c. Further details on the c-shaped waveguide propagation are reported in the Appendix A.

From the analysis of these results it emerges that, in practice, cutoff frequencies well within the K/Ka-band can be obtained with small values of w (in the order of 2 mm or so), thus parasitic c-waveguides should be carefully taken into account during the layout design.

B. GROUND VIA SPACING

The amount of feedback through the c-shaped waveguide in Fig. 4(a) is related to the signal that leaks-out of the via rows delimiting the transmission line, i.e. either a grounded CPW or a SIW in our case. Such a signal is usually faint, but it can turn into a problem if the amplifier gain is high. The radiation leakage due to the side vias of a SIW section was studied in [37], [38]. Without loss of generality, also the present analysis focuses on the SIW technology. Following [37], the attenuation constant α_R due to the SIW radiation is related to the geometry by:

$$\alpha_R \approx \frac{1}{20\,\log_{10} e}\,\frac{\frac{1}{a}\left(\frac{d}{a}\right)^{2.84}\left(\frac{s}{d}-1\right)^{6.28}}{4.85\sqrt{\left(\frac{2a}{\lambda}\right)^2-1}} \tag{3}$$

where a is the waveguide width, d is the via diameter, s is the via spacing and $\lambda = c_0/(\sqrt{\epsilon_R} f)$ is the wavelength in the dielectric medium at the operating frequency f. The factor $1/(20\,\log_{10} e)$ is used to convert the attenuation factor expressed in dB/m, [37], into the attenuation constant given

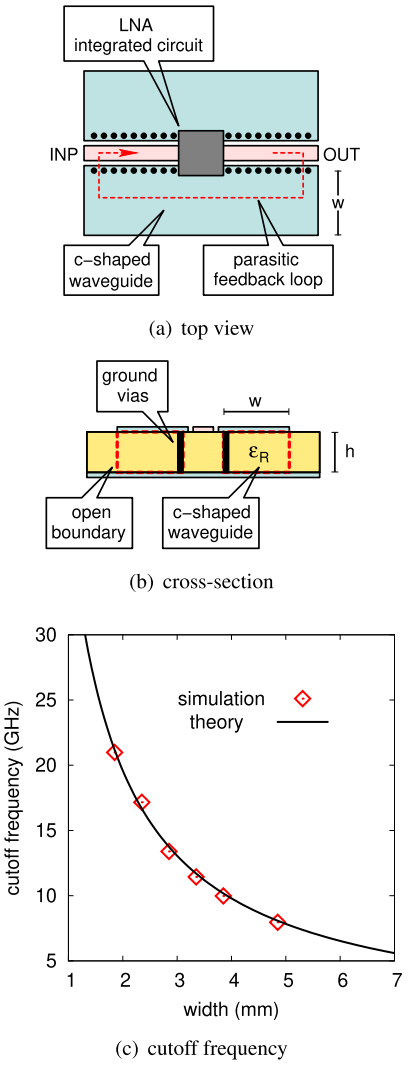

FIGURE 4. Unwanted feedback loop that can arise between output and input of an integrated LNA. This loop is established, via the PCB, through a parasitic c-shaped waveguide as in (a). The structure cross-section is shown in (b), w being the waveguide width, h the substrate height and ϵ_R the relative permittivity. Although such a structure has an open boundary (and it is lossy due to radiation), it can propagate a signal back to the input destabilizing the amplifier. The cutoff frequency is represented in (c) for a substrate with $h = 0.25$ mm and $\epsilon_R = 3.66$. Here a simple theoretical model (see text) is compared with electromagnetic simulations (agreement within ±3%).

in 1/m. Now, considering a waveguide section of length l, the transmission coefficient T can be written as:

$$T = \exp(-\alpha_R\, l) \tag{4}$$

and the fraction of power p_r that leaks out of the via is:

$$p_r = 1 - T^2 \approx 2\,\alpha_R\, l \tag{5}$$

Note that the last approximation is valid for small values of α_R, which is applicable to the studied case. Combining (5) with (3) it is possible to estimate the leak-out power fraction as a function of the via spacing. For example, considering the waveguide adopted in the image rejection filters (see

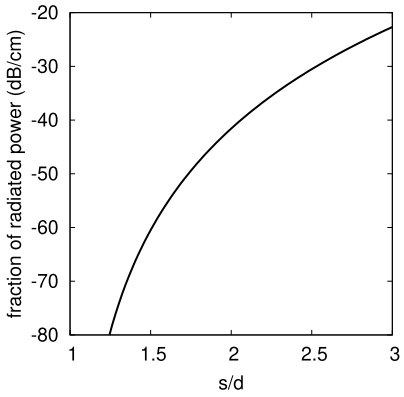

FIGURE 5. Leak-out power fraction in dB as a function of s/d for $f = 29$ GHz. SIW parameters: $a = 4$ mm, $d = 0.3$ mm, $\epsilon_R = 3.66$. The power fraction p_r is estimated for a 1-cm waveguide section.

next section), we have the following parameters: $a = 4$ mm, $d = 0.3$ mm, $l = 1$ cm, $\epsilon_R = 3.66$ and $f = 29$ GHz. Under these conditions, the behavior shown in Fig. 5 is obtained.

As it can be seen, for a typical $s/d = 2$ the power leakage is close to -40 dB/cm, which is not negligible for high gain amplifiers like that used in the described front-end. To further reduce the leakage, double rows of closely spaced ground vias are adopted.

C. PCB MODELING AND LNA CO-SIMULATION

The parasitic output-to-input feedback discussed previously is due to the signal traveling within the PCB. Another important coupling mechanism, however, is due to radiation. In both cases the separation distance d that exists between the two LNA stages is an important parameter. Increasing the distance can reduce the parasitic coupling, and this is fundamental to achieve the unconditional stability without shields. Placing the image rejection filter between the two amplifiers we can increase d without wasting space, see Fig. 6(a). An important consequence of this choice is that the amplifier stability is also positively affected by the filter losses.

To model all the above effects 6 PCB ports have been identified, as depicted in Fig. 6(b). Ports 1 and 2 are external and represent the input/output interfaces of the circuit. The remaining four ports (namely port 3, 4, 5 and 6) are the internal terminals where the integrated circuits are connected. Then, the 6-ports scattering matrix of the PCB is evaluated with a 3D CST electromagnetic simulator. Such a matrix is then combined with the measured scattering parameters of the two LNA integrated circuits, which are generally provided by the vendors. The resulting (equivalent) network representation is illustrated in Fig. 6(c) and combines together numerical PCB model and integrated circuit measurements.

The amplifier frequency response is evaluated exploiting the above network representation. To illustrate the co-simulation procedure, a 4-cavities SIW filter is considered (see Sec. VI for further details about this filter). The first

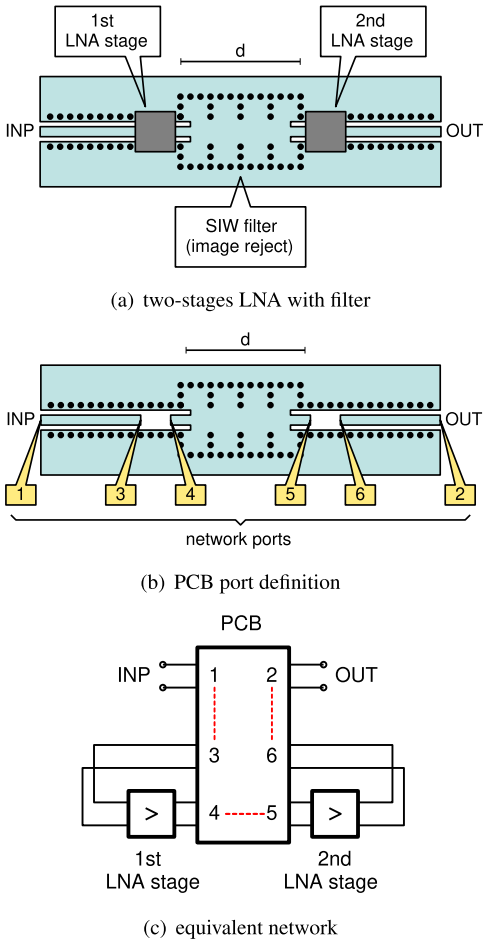

FIGURE 6. Modeling of the two-stages LNA with interstage SIW filter (a). In a first step the two LNA integrated circuits are removed and 6 ports are identified (b). Then the 6-ports scattering matrix of the PCB is evaluated with an electromagnetic simulator. Such a matrix is finally combined with the LNA measurements (scattering parameters provided by the vendor) in such a way as to get an equivalent network (c). This representation allows for the two-stages LNA frequency response evaluation, including the PCB behavior. Note that the latter accounts for both the SIW filter frequency response and all the parasitic coupling effects (both radiated and conducted by the PCB itself).

stage is constituted by the HMC1044, while the second stage is the HMC566; both the integrated circuits are from Analog Devices. The obtained small-signal gain is shown in Fig. 7: the filter frequency response is clearly visible and a peak gain equal to 42.4 dB is reached at 28.3 GHz. The amplifier stability is discussed starting from the scattering parameters. The μ stability factor is evaluated as:

$$\mu = \frac{1 - |S_{11}|^2}{|S_{22} - \Delta\, S_{11}^*| + |S_{12}\, S_{21}|} \tag{6}$$

where S_{ij} with $i, j = 1, 2$ are the scattering parameters of the circuit and $\Delta = S_{11}\, S_{22} - S_{12}\, S_{21}$ is the scattering matrix determinant. The μ factor is plotted again in Fig. 7 and, as it can be seen, it is always greater than one, testifying the unconditional stability of the designed circuit.

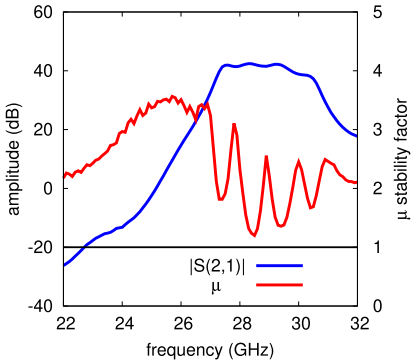

FIGURE 7. Co-simulation of a two-stages LNA with interstage 4-cavities SIW image rejection filter. $|S_{21}|$, or small-signal transducer power gain referred to 50 Ω, and μ stability factor. First stage: HMC1044; second stage: HMC566; both the integrated circuits are from Analog Devices. The peak gain is 42.4 dB at 28.3 GHz and the circuit is unconditionally stable.

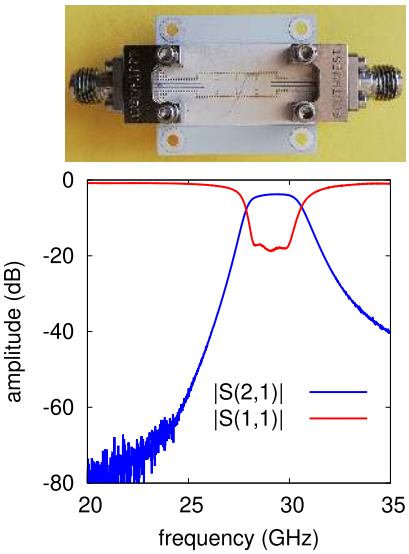

FIGURE 8. 4-cavities image rejection filter implemented in SIW technology: layout (top) and experiments (bottom). The filter is realized on RO4350B with $h = 0.25$ mm, $\epsilon_R = 3.66$ and $\tan\delta = 0.004$. The measured insertion loss at 29.15 GHz is 3.6 dB, including the feeding lines and the two coaxial-to-CPW end launchers. The return loss is around 20 dB at center frequency. A 60 dB rejection is obtained between 23 and 26 GHz.

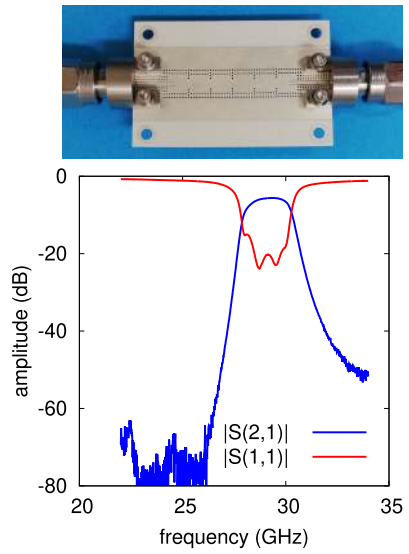

FIGURE 9. 6-cavities image rejection filter implemented in SIW technology: layout (top) and experiments (bottom). The filter is realized on RO4350B with $h = 0.25$ mm, $\epsilon_R = 3.66$ and $\tan\delta = 0.004$. The measured insertion loss at 29.15 GHz is 5.6 dB, including the feeding lines and the two coaxial-to-CPW end launchers. The return loss is better than 20 dB at center frequency. A 70 dB rejection is obtained between 23 and 26 GHz.

VI. RESULTS

Two proof-of-concept image rejection filters have been manufactured in SIW technology using a low-cost RO4350B substrate. The filters are designed according to [6] and are centered at 29.15 GHz. The design procedure is quite standard and will not repeated here; we simply note that, in order to speed-up such a procedure, an automatic layout generation similar to that reported in [39] could be adopted, along with full-wave electromagnetic solvers [40].

Fig. 8 represents the first filter and the corresponding scattering parameters (measurements). Such a filter (overall length 28 mm) exploits 4 iris-coupled cavities and it is fed by two 50 Ω grounded CPW transmission lines. The insertion loss is 3.6 dB, including the feeding lines and the two launchers, whereas the return loss is around 20 dB at center frequency. A 60 dB rejection is obtained between 23 and 26 GHz.

To improve the low-frequency rejection, a 6-cavities SIW filter has also been designed, implemented and experimentally characterized. This second filter (overall length 36 mm) is illustrated in Fig. 9. The measured insertion loss is 5.6 dB, including the feeding lines and the two coaxial adapters, and a return loss better than 20 dB at center frequency is obtained. A 70 dB rejection is obtained between 23 and 26 GHz. These two experiments show that the SIW technology is mature and reliable for Ka-band space applications, even with the adoption of a low-cost dielectric substrate like the Rogers RO4350B. Furthermore, several prototypes of both the 4- and 6-cavities filters have been fabricated (exploiting an external service) and measured. The obtained frequency responses are very close to each other, demonstrating that the tolerances of a commercial PCB fabrication process are adequate for the target application.

In order to validate the approach developed in Sec. V, an LNA board is implemented, as shown in Fig. 10. As already stated, the LNA uses the HMC1040 device as the first stage and the HMC566 device as the second stage. The two different integrated circuits have been selected considering their frequency responses, so as to obtain a maximally flat gain in the pass band. A compensation is obtained since the HMC1040 gain decreases by about 2 dB between 27.5 and 30 GHz, whereas that of the HMC566 increases by almost the same quantity. Furthermore, at the considered frequencies, the HMC1040 has a gain of about 25 dB while

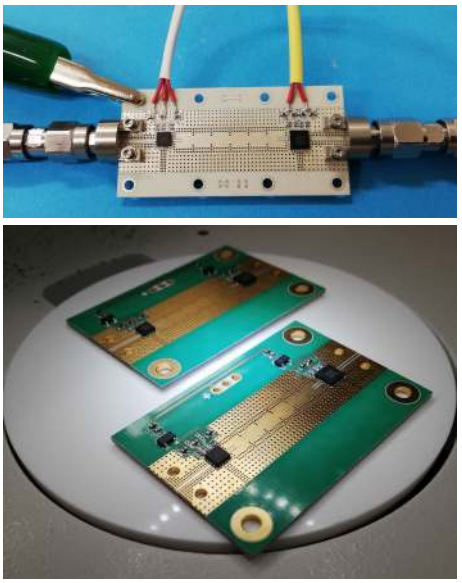

FIGURE 10. Implemented two-stages LNA board with 6-cavities interstage SIW filter. Laboratory prototype (top) and engineered version (bottom). The first stage (to the left) is the HMC1040 while the HMC566 is used as the second stage (right). The LNA board is implemented on RO4350B with $h = 0.25$ mm, $\epsilon_R = 3.66$ and $\tan\delta = 0.004$. The first stage current is 70 mA at 2.5 V, while the second stage consumption is 82 mA at 3 V. The overall power consumption is around 0.42 W. The PCB size (connectors not included) is 42 mm in length and 24 mm in height.

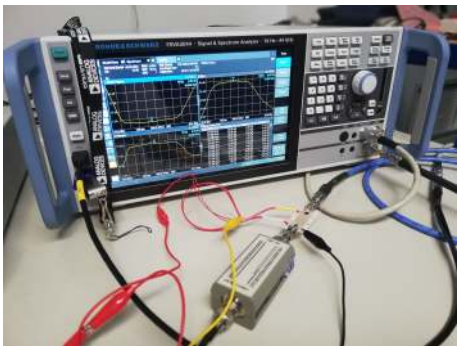

FIGURE 11. Experimental setup used for the determination of the LNA noise-figure and available power gain with the Y-factor method. a Rode&Schwarz Spectrum Analyzer (FSVA3044 up to 44 GHz with internal preamplifier) and a 346C-K01 solid-state noise source form Keysight technologies have been used to this purpose.

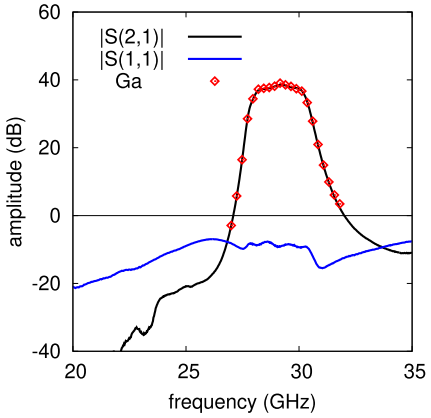

FIGURE 12. Measured scattering parameters of the LNA board. The peak gain is equal to 38.5 dB at 29.15 GHz, the input reflection coefficient magnitude is around −9 dB in the operation bandwidth, whereas the rejection is better than 80 dBc between 20 and 23 GHz. As a cross check, the available power gain G_a measured with the Y-factor method (see below), is plotted above the $|S_{21}|$ curve, showing an excellent agreement.

the HMC566 gain is 20 dB. As a consequence the overall gain can be close to 40 dB when the 6-cavities filter is adopted.

The prototype LNA board is implemented with the same substrate used for the filters (Rogers RO4350B) while two 2.92-mm coaxial-to-CPW adapters (type ELF40-001 from Signal Microwave) are used to provide the external connections. The first stage draws a 70 mA current at 2.5 V; the second-stage current consumption, instead, is 82 mA at 3 V. The overall power required by the LNA is around 0.42 W.

The LNA characterization is carried out in two steps. First, the scattering parameters are measured as a function of the frequency with a Vector Network Analyzer (VNA), model Agilent Technologies N5230A up to 40 GHz, equipped with an electronic calibration kit. Then the noise figure is determined with the Y-factor method [41], using a Rode&Schwarz Spectrum Analyzer, model FSVA3044 up to 44 GHz (with internal preamplifier) and a 346C-K01 solid-state noise source from Keysight Technologies. Such an experimental set-up is shown in Fig. 11. Finally, to cross-check the two methods, the available power gain obtained with the Y-factor is compared to the $|S_{21}|$ measured by the VNA.

The experimental results obtained with the above approach are illustrated in Fig. 12 and in Fig. 13. From these measurements emerges that the peak gain is 38.5 dB at 29.15 GHz with an input reflection coefficient around −9 dB in the whole operation bandwidth. The image rejection is better than 80 dBc between 20 and 23 GHz. The LNA reaches a 2.8 ± 0.6 dB noise figure at 29.15 GHz; such a value includes the insertion losses due to the 2.92-mm adapters. Note that the noise figure uncertainty is assumed equal to the sum between the instrument uncertainty in Y-factor mode (± 0.1 dB) and to the estimated mismatch loss (± 0.5 dB). The comparison between $|S_{21}|$ and the available power gain G_a measured with the Y-factor is excellent (see Fig. 12).

Fig. 14 represents μ stability factor versus the frequency obtained applying (6) to the measured scattering matrix of the amplifier. The stability factor is always greater than 1, thus ensuring the unconditional stability of the developed LNA.

The down-converter board was realized according to the block diagram of Fig. 2. Such a board operates in the Ka-band between 27.5 and 30 GHz. The 3.7 GHz IF signal is obtained using a sub-harmonically pumped mixer. The LO is in the 11.90 to 13.15 GHz range and is generated by a single-chip PLL synthesizer. An analog Automatic Gain Control (AGC) loop is provided in the down-converter (not shown in Fig. 2). It is consitituted by a RFSA2113 Voltage Controlled Attenuator (VCA) placed between the third and the fourth IF stage and by an ADL5902 true rms responding

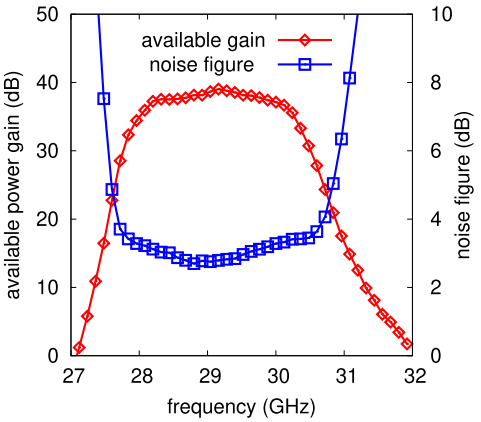

FIGURE 13. Available power gain and noise figure of the LNA board measured with the Y-factor method. The peak gain is 39 dB at 29.15 GHz, while the minimum noise figure is 2.8 ± 0.5 dB at the same frequency. This value also includes the insertion losses due to the 2.92 mm ELF40-001 coaxial adapters.

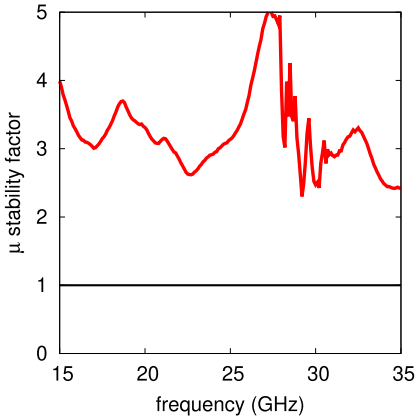

FIGURE 14. Stability factor μ of the LNA extracted from the measured scattering parameters. The developed amplifier is unconditionally stable since $\mu > 1$ in the whole frequency band.

power detector. The AGC loop can be closed or opened with a jumper and, in a future down-converter version, it could also be actuated via a microcontroller. The down-converter is shown in Fig. 15 and fits within a one-unit (1U) CubeSat. The overall current consumption is 560 mA at 5 V, thus resulting in a power of 2.8 W.

The down-converter gain was measured in Continuous Wave (CW) mode: a 28.91 GHz input is provided to the board with RF Vector Signal Generator (Rode&Schwarz SMW200A) and, correspondingly, the 3.7 GHz IF output is measured with a Spectrum Analyzer (Rode&Schwarz FSW up to 43 GHz). At the same time, the detector output voltage is also recorded in order to identify the AGC threshold. These measurements are reported in Fig. 16, showing an available power gain of 48 dB and an AGC input threshold equal to −65 dBm. In these conditions the output IF power kept constant at −13 dBm.

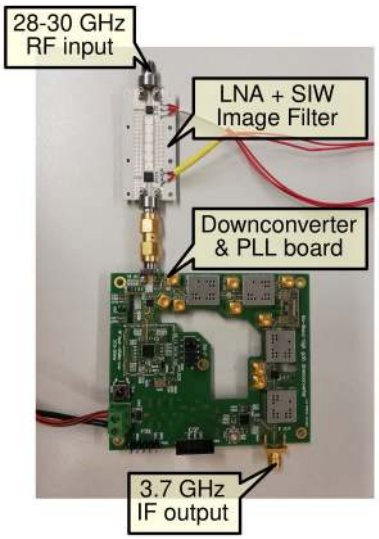

FIGURE 15. Ka-band front-end breadboard. This is constituted by the connection between the LNA and the down-converter boards.The down-converter also includes the PLL synthesizer (local oscillator) and the 3.7 GHz IF chain.

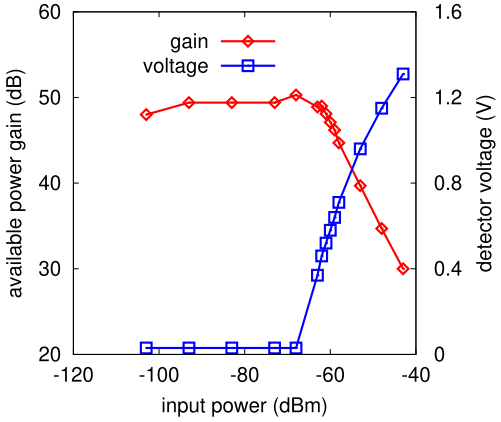

FIGURE 16. Down-converter gain with closed AGC loop and detector control voltage versus the input available power. Test conditions: RF frequency 28.91 GHz; IF frequency 3.71 GHz. The overall gain is around 48 dB and the input AGC threshold equal to −65 dBm. The AGC is designed to keep the output IF power level below −13 dBm.

TABLE 2. Ka-band receivers for space applications state-of-the-art.

Ref.	Mission Scenario	f_0 (GHz)	Gain (dB)	F_{RX} (dB)	DC (W)	Mass (kg)
[42]	International Space Station	22.5-23.1	n.a.	2.3	n.a.	19.2 (*)
[43]	GEO satellites	27.5-31.0	55	2.3	5.0	0.2
this work	LEO to GEO CubeSats ISL	27.5-30.0	80	2.8	3.2	0.4

(*) includes a 40 W transmitter unit

Finally, the overall front-end (LNA and down-converter), is characterized by measuring the output IF spectrum (with 10 kHz resolution bandwidth), as reported in Fig. 17(a).

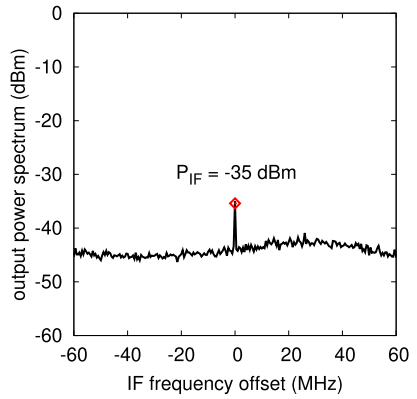

(a) output power spectrum, $P_{in} = -115$ dBm

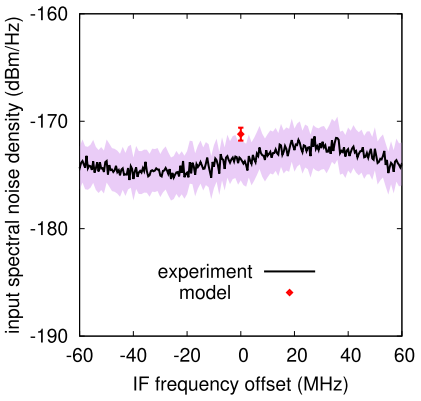

(b) input referred spectral noise density

FIGURE 17. Test of the whole Ka-band front-end, i.e. LNA and down-converter boards connected together. Output power spectrum versus the IF frequency offset with respect to 3.7 GHz, (a). Test conditions: RF frequency 28.91 GHz, available input power −115 dBm (this value is compensated accounting for cable losses), output IF level equal to −35 dBm. The overall front-end gain with AGC loop is around 80 dB. In the same conditions also the input referred spectral noise density is measured, (b). To this purpose the front-end input is terminated on a 50 Ω load at ambient temperature. The most likely value at the IF center frequency is: −173.5 ± 2 dBm/Hz (confidence limits also shown in the graph). This value is compatible, within the experimental uncertainty, with the measured 2.8 dB noise figure (red point and related error bars).

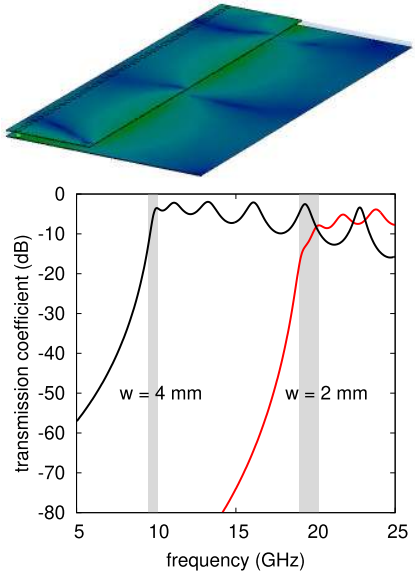

FIGURE 18. Numerical simulation of the c-shaped waveguide: surface currents (top panel) and transmission coefficients (bottom panel). The structure, which is 20 mm long, uses a dielectric material with $h = 0.25$ mm and $\epsilon_R = 3.66$ (dielectric loss neglected). The transmission coefficients are computed for w equal to 4 and 2 mm and are normalized to 50 Ω. The two gray boxes represent the cutoff frequencies evaluated with the proposed equation ±3%.

In particular, a 28.91 GHz CW is applied to the front-end input. The available power is set to −115 dBm (−110 dBm SMW200A output, cable loss equal to 5 dB) and, in these conditions, the delivered IF power at 3.7 GHz is −35 dBm (see marker). As a result, the overall transducer power gain is around 80 ± 1.2 dB, where ±1.2 dB is the level uncertainty of the SMW200A signal generator. Note that this value is 6 dB lower than the one obtained considering the gains of LNA and down-converter separately (i.e. 38 + 48 = 86 dB). Such a discrepancy is due to the amplified wideband noise in the AGC loop. The detected noise power, indeed, produces a voltage that is fed back to the VCA, actuates the attenuator and, as a consequence, reduces the gain.

The front-end output-referred spectral noise density is equal to −94.3 dBm/Hz. Such a value is obtained using the Spectrum Analyzer noise marker with 0 dB attenuation and 100 averaged measurements. In this experiment the front-end input is terminated on a 50 Ω SMA load (−17 dB return loss in the Ka-band) at ambient temperature, while the PLL is set to receive a 28.91 GHz signal.

Such a spectral noise density, however, should be corrected accounting for 0.8 dB output cable loss and its most likely value is −93.5 dBm/Hz. The uncertainty of such a value is estimated in ±0.8 dB; 0.4 dB due to the FSW43 Spectrum Analyzer accuracy and 0.4 dB associated to the input mismatch uncertainty [41, p. 22]. The corrected spectral noise density is this −93.5 ± 0.8 dBm/Hz.

The input-referred spectral noise density can be estimated equal to −173.5 ± 2 dBm/Hz, a value obtained subtracting the front-end gain to the above output noise density, see Fig. 17(b). Such a value is compatible, within the experimental uncertainty, with a 2.8 ± 0.6 dB noise figure, indeed we have −174 + 2.8 ± 0.6 = −171.2 ± 0.6 dBm/Hz (red point indicated to as "model" in the figure).

Finally, a comparison with the state-of-the-art for K/Ka band receiver front-ends is illustrated in Tab. 2. All the considered receivers are conceived for space applications. The proposed front-end compares well with two relevant designs, the first from Harris Downey *et al.* [42] (that, however, operates in the K-band, i.e. at a lower frequency) and the second from Alenia Sapce [43].

The developed receiver shows the highest gain, whereas the noise figure is in line with that of the other published designs. To this purpose, however, we have to note that the reported 2.8 dB value includes the insertion loss of the 2.92-mm adapter; the latter being estimated around 0.5 dB.

The front-end power consumption is equal to 3.2 W (sum of the 0.42 W LNA power with the 2.8 W down-converter power) and is 56% lower than that reported in [43]. Mass and size are suitable for CubeSats applications: the down-converter board has an aspect ratio compatible with a one-unit module, while the LNA board can be mounted atop the down-converter.

VII. CONCLUSION

In the next years the space community is planning to exploit the existing FSS network based on GEO satellites to facilitate the communication between Earth and small LEO satellites. As a consequence Inter-Satellite Links (ISL) between LEO and GEO are currently under study to provide high-data rates and high coverage, particularly for the emerging CubeSats market.

The feasibility of a Ka-band, high data rate receiver for CubeSats ISL applications was investigated in the present contribution, and different strategies have been proposed to overcome implementation issues. Firstly, it was shown that COTS integrated circuits and SIW technology can be used to reduce the electronic hardware cost as well as the need for shielding apparatuses. An optimization of the via placement is used to further reduce the power leakage from the output to the input of the LNA, thus simplifying the mechanics and reducing mass, volume and hardware costs. Furthermore a gain calibration circuitry based on noise injection was successfully investigated. This circuitry can provide a self testing capability, an option relevant for space applications where the usage of commercial components poses serious reliability issues. Finally, to validate the above concepts, a preliminary front-end breadboard operating between 27.5 and 30 GHz was implemented. The breadboard exploits custom PCBs and features a 80 dB gain, a 2.8 dB noise figure and an image rejection greater than 70 dBc. These results set a new state-of-the-art for Ka-band active front-ends based on SIW technology.

ACKNOWLEDGMENT

The authors are particularly grateful to Rodhe&Schwarz Italia (Alessandro Titta, Andrea Saliciotti and Massimo Bauco) for the support during the LNA characterization. Paolo Gervasoni, Paolo Glionna and Alessia Ruggeri of Analog Devices are acknowledged for the donation of many evaluation-boards and integrated circuits samples. Federico Pergolesi is also acknowledged for having contributed to the front-end design, when he was with PicoSaTs s.r.l.

APPENDIX A
SIMULATION OF THE C-SHAPED WAVEGUIDE

The c-shaped waveguide is modeled with an electromagnetic simulator (i.e. CST) as in Fig. 18 (top panel). In this case the open boundary is truly radiating, and the magnetic wall approximation is not used. As in the presented study, a dielectric material with $h = 0.25$ mm, $\epsilon_R = 3.66$ is considered, but the dielectric losses (i.e. $\tan\delta$) are neglected. The structure is 20 mm long and, for the evaluation of the scattering parameters, it is excited/terminated with a 50 Ω source/resistor. These "lumped-element" ports are located at the open-edge of the structure to excite the fundamental mode. The computed transmission coefficient are reported in Fig. 18 (bottom panel) for two w values, namely 2 and 4 mm. The cutoff frequency with $w = 2$ mm is in agreement with the 19.6 GHz value evaluated by eqn. (2) whereas, with $w = 4$ mm, such a value is reduced by a factor 2.

It is interesting to note that, although radiating (see the surface currents in the top figure panel), the transmission coefficients of the c-shaped waveguide is quite high (it reaches the −5 dB level in the peaks), testifying the propagation characteristics of the structure.

REFERENCES

[1] F. Berrilli, A. Bigazzi, L. Roselli, P. Sabatini, M. Velli, F. Alimenti, F. Cavallini, V. Greco, P. Moretti, S. Orsini, M. Romoli, S. White, and ADAHELI Team, "The ADAHELI solar mission: Investigating the structure of the sun's lower atmosphere," *Adv. Space Res.*, vol. 45, no. 10, p. 1191–1202, May 2010.

[2] National Academies of Sciences, Engineering, and Medicine, "Achieving science with CubeSats: Thinking inside the box," Nat. Acad. Press, Washington, DC, USA, White Paper, 2016, doi: 10.17226/23503.

[3] M. Mitry, "Routers in space: Kepler communications' CubeSats will create an Internet for other satellites," *IEEE Spectr.*, vol. 57, no. 2, pp. 38–43, Feb. 2020.

[4] A. Cuttin, F. Alimenti, F. Coromina, E. De Fazio, F. Dogo, M. Fragiacomo, P. Gervasoni, G. Gotti, A. Gregorio, P. Mezzanotte, E. Pagana, V. Palazzi, F. Pelusi, P. Petrini, L. Roselli, and R. V. Gatti, "A Ka-band transceiver for CubeSat satellites: Feasibility study and prototype development," in *Proc. 48th Eur. Microw. Conf. (EuMC)*, Madrid, Spain, Sep. 2018, pp. 1–4.

[5] A. Gregorio and F. Alimenti, "CubeSats for future science and Internet of space: Challenges and opportunities," in *Proc. 25th IEEE Int. Conf. Electron., Circuits Syst. (ICECS)*, Bordeaux, France, Dec. 2018.

[6] X.-P. Chen and K. Wu, "Substrate integrated waveguide cross-coupled filter with negative coupling structure," *IEEE Trans. Microw. Theory Techn.*, vol. 56, no. 1, pp. 142–149, Jan. 2008.

[7] H. Tang, Y. Zhang, and W. Hong, "Realization of a sub-harmonic mixer with a substrate integrated waveguide filter," in *Proc. IEEE/ACES Int. Conf. Wireless Commun. Appl. Comput. Electromagn.*, Honolulu, HI, USA, Apr. 2005, pp. 779–782.

[8] Y.-W. Wang, J.-Y. Zhou, and W. Hong, "Study of dual-balanced mixer with half mode substrate integrated waveguide," in *Proc. Int. Conf. Microw. Millim. Wave Technol.*, Nanjing, China, Apr. 2008, pp. 1509–1511.

[9] Z. Zhang, K. Wu, and Y. Wei, "180-degree substrate integrated waveguide hybrid and its application to broadband millimeter-wave single balanced mixer design," in *Proc. Asia–Pacific Microw. Conf. (APMC)*, Yokohama, Japan, Dec. 2010, pp. 1649–1652.

[10] A. Collado, R. Diaz, and A. Georgiadis, "X-band substrate integrated waveguide (SIW) active antenna self-oscillating mixer (SOM)," in *Proc. IEEE Int. Symp. Antennas Propag.*, Chicago, IL, USA, Jul. 2012, pp. 1–2.

[11] A. Georgiadis, A. Collado, and K. Niotaki, "22.8 GHz substrate integrated waveguide analog frequency Divide-by-3 circuit," *IEEE Microw. Wireless Compon. Lett.*, vol. 25, no. 5, pp. 304–306, May 2015.

[12] M. Abdolhamidi and M. Shahabadi, "X-band substrate integrated waveguide amplifier," *IEEE Microw. Wireless Compon. Lett.*, vol. 18, no. 12, pp. 815–817, Dec. 2008.

[13] F. Taringou, J. Bornemann, and K. Wu, "Broadband coplanar-waveguide and microstrip low-noise amplifier hybrid integrations for K-band substrate integrated waveguide applications on low-permittivity substrate," *IET Microw., Antennas Propag.*, vol. 8, no. 2, pp. 99–103, Jan. 2014.

[14] K. Eccleston, "Effect of microstrip feeds on half-mode SIW distributed amplifier performance," in *Proc. IEEE Asia–Pacific Microw. Conf. (APMC)*, Nanjing, China, Dec. 2015, pp. 1–3.

[15] K. W. Eccleston, "SIW distributed amplifier: Analysis, prospects and challenges," in *Proc. IEEE MTT-S Int. Conf. Numer. Electromagn. Multiphys. Model. Optim. (NEMO)*, Beijng, China, Jul. 2016, pp. 1–2.

[16] Z. Wang, S. Adhikari, D. Dousset, C. Park, and K. Wu, "Substrate integrated waveguide (SIW) power amplifier using CBCPW-to-SIW transition for matching network," in *IEEE MTT-S Int. Microw. Symp. Dig.*, Montreal, QC, Canada, Jun. 2012, pp. 1–3.
[17] Z. Wang and C.-W. Park, "Novel substrate integrated waveguide (SIW)-based power amplifier using SIW-based filter to suppress up to the fourth harmonic," in *Proc. Asia–Pacific Microw. Conf.*, Kaohsiung, Taiwan, Dec. 2012, pp. 830–832.
[18] Z. Wang and C.-W. Park, "Novel substrate integrated waveguide (SIW) type high power amplifier using microstrip-to-SIW transition," in *Proc. Asia–Pacific Microw. Conf. Proc. (APMC)*, Kaohsiung, Taiwan, Nov. 2013, pp. 830–832.
[19] D. T. J. Diatta and C.-W. Park, "Full mode substrate integrated waveguide type high power amplifier with second harmonic suppression," in *Proc. IEEE Asia–Pacific Microw. Conf. (APMC)*, Lumpur, Malaysia, Nov. 2017, pp. 992–994.
[20] W. Feng, Y. Shi, X. Y. Zhou, X. Shen, and W. Che, "A bandpass push–pull high power amplifier based on SIW filtering balun power divider," *IEEE Trans. Plasma Sci.*, vol. 47, no. 9, pp. 4281–4286, Sep. 2019.
[21] K. K. Samanta, D. Stephens, and I. D. Robertson, "60 GHz multi-chip-module receiver with substrate integrated waveguide antenna and filter," *Electron. Lett.*, vol. 42, no. 12, pp. 701–702, Jun. 2006.
[22] K. K. Samanta, D. Stephens, and I. D. Robertson, "Design and performance of a 60-GHz multi-chip module receiver employing substrate integrated waveguides," *IET Microw., Antennas Propag.*, vol. 1, no. 5, pp. 961–967, Oct. 2007.
[23] S. Sun and Y. Huang, "Design of a 60 GHz receiver RF front-end integrated with substrate integrated waveguide," in *Proc. 31st URSI Gen. Assem. Sci. Symp. (URSI GASS)*, Beijing, China, Aug. 2014, pp. 1–4.
[24] D. Deslandes and K. Wu, "High isolation substrate integrated waveguide passive front-end for millimeter-wave systems," in *IEEE MTT-S Int. Microw. Symp. Dig.*, San Francisco, CA, USA, Jun. 2006, pp. 982–985.
[25] T. Djerafi, M. Daigle, H. Boutayeb, X. Zhang, and K. Wu, "Substrate integrated waveguide six-port broadband front-end circuit for millimeter-wave radio and radar systems," in *Proc. Eur. Microw. Conf. (EuMC)*, Rome, Italy, Sep. 2009, pp. 77–80.
[26] K. K. Samanta, "Advanced multilayer photoimaged substrate integrated waveguides and RF front-end for emerging mm-wave wireless applications," in *Proc. IEEE Topical Conf. Wireless Sensors Sensor Netw. (WiSNet)*, Jan. 2014, pp. 16–18.
[27] F. Alimenti *et al.*, "K/Ka-band very high data-rate receivers: A viable solution for future Moon exploration missions," *MDPI Electron.*, vol. 8, no. 3, pp. 1–23, Mar. 2019.
[28] Y. Rahmat-Samii, V. Manohar, and J. M. Kovitz, "For satellites, think small, dream big: A review of recent antenna developments for CubeSats.," *IEEE Antennas Propag. Mag.*, vol. 59, no. 2, pp. 22–30, Apr. 2017.
[29] N. E. Chahat, "A mighty antenna from a tiny CubeSat grows," *IEEE Spectr.*, vol. 55, no. 2, pp. 32–37, Feb. 2018.
[30] F. Alimenti, P. Mezzanotte, V. Palazzi, L. Roselli, F. Dogo, and M. Fragiacomo, "Dispositivo ricevitore a microonde," Italy Patent 102 020 000 008 773, Apr. 23, 2020.
[31] J. Knogl, "Geostationary data relays for low earth orbit satellites," Ph.D. dissertation, Fakultät für Elektrotechnik und Informationstechnik, Lehrstuhl für Kommunikation und Navigat., Tech. Univ. Munich, Munich, Germany, Jun. 2014.
[32] F. Alimenti, G. Tasselli, C. Botteron, P.-A. Farine, and C. Enz, "Avalanche noise diodes: A compact circuit model compatible with advanced CAD tools," in *Proc. Int. Conf. Noise Fluctuations (ICNF)*, Xi'an, China, Jun. 2015, pp. 1–4.
[33] G.-P. Hu, Y.-C. Zheng, A.-A. Xu, and Z.-S. Tang, "Microwave brightness temperature of the moon: The possibility of setting a calibration source of the lunar surface," *IEEE Geosci. Remote Sens. Lett.*, vol. 13, no. 2, pp. 182–186, Feb. 2016.
[34] M. C. Maya, A. Lázaro, and L. Pradell, "Extraction of an avalanche diode noise model for its application as an on-wafer noise source," *Microw. Opt. Technol. Lett.*, vol. 38, no. 2, pp. 89–92, Jul. 2003.
[35] F. Alimenti, G. Tasselli, C. Botteron, P.-A. Farine, and C. Enz, "Avalanche microwave noise sources in commercial 90-nm CMOS technology," *IEEE Trans. Microw. Theory Techn.*, vol. 64, no. 5, pp. 1409–1418, May 2016.
[36] C. Emili, F. Alimenti, P. Mezranotte, L. Roselli, and R. Sorrentino, "Rigorous modeling of packaged Schottky diodes by the nonlinear lumped network (NL^2N)-FDTD approach," *IEEE Trans. Microw. Theory Techn.*, vol. 48, no. 12, pp. 2277–2282, Dec. 2000.
[37] M. Pasian, M. Bozzi, and L. Perregrini, "Radiation losses in substrate integrated waveguides: A semi-analytical approach for a quantitative determination," in *IEEE MTT-S Int. Microw. Symp. Dig.*, Seattle, WA, USA, Jun. 2013, pp. 1–3.
[38] M. Bozzi, M. Pasian, and L. Perregrini, "Advanced modeling and design of substrate integrated waveguide components," in *Proc. IEEE Int. Wireless Symp. (IWS)*, Xian, China, Mar. 2014, pp. 1–4.
[39] L. Aluigi, F. Alimenti, D. Pepe, L. Roselli, and D. Zito, "MIDAS: Automated approach to design microwave integrated inductors and transformers on silicon," *Radioengineering*, vol. 22, no. 3, pp. 714–723, Sep. 2013.
[40] F. Alimenti, P. Mezzanotte, L. Roselli, and R. Sorrentino, "Efficient analysis of waveguide components by FDTD combined with time domain modal expansion," *IEEE Microw. Guided Wave Lett.*, vol. 5, no. 10, pp. 351–353, Oct. 1995.
[41] Fundamental of RF and Microwave Noise Figure Measurements. Agilent Technologies, 2000. [Online]. Available: http://www.agilent.com
[42] J. Downey and T. Kacpura, "Pre-flight testing and performance of a Ka-band software defined radio," in *Proc. 30th AIAA Int. Commun. Satell. Syst. Conf. (ICSSC)*, Ottawa, ON, Canada, Sep. 2012, pp. 1–13.
[43] M. C. Comparini, M. Feudale, J. R. Linkowski, P. Ranieri, and A. Suriani, "Fully integrated Ka/K band hermetic receiver module," in *Proc. 30th Eur. Microw. Conf.*, Paris, France, Oct. 2000.

FEDERICO ALIMENTI (Senior Member, IEEE) received the Laurea *(magna cum laude)* and Ph.D. degrees in electronics engineering from the University of Perugia, Italy, in 1993 and 1997, respectively. In 1996, he was a recipient of the URSI Young Scientist Award and a Visiting Scientist at the Technical University of Munich, Germany. Since 2001, he has been with the Department of Engineering, University of Perugia, teaching the class of RFIC design. From 2011 to 2014, he was the Scientific Coordinator of the ENIAC ARTEMOS Project. In 2013, he was the recipient of the IET Premium (Best Paper) Award and the TPC Chair of the IEEE Wireless Power Transfer Conference. In the summer 2014, he was a Visiting Professor at EPFL, Switzerland. He has participated at the Summer School, in 2017, held at Infineon Austria AG, Villach, as a Keynote Lecturer. In 2018, he got the qualification as a Full Professor and won the Mario Sannino Award for the best research in the field of microwave electronics. He holds a European patent (EP2660755) and has authored more than 200 articles in journals, conferences, and books. His h-index is 20 with more than 1500 citations (source Scopus) and 23 with more than 2000 citations (source Google Scholar). His interests include microwave and RFIC design.

PAOLO MEZZANOTTE (Member, IEEE) was born in Perugia, Italy, in 1965. He received the Ph.D. degree from the University of Perugia, Perugia, in 1997. Since 2007, he has been an Associate Professor with the University of Perugia, where he has been involved in teaching the classes of radio-frequencies engineering and systems and circuits for the IoT. Since 2014, he has been the Vice Head of the Department of Engineering, University of Perugia. His present h-index is 24. His research activities are testified by over 170 publications in the most reputed specialized journals and at the main conferences of the microwave scientific community. His current research interests include the development of microwave circuits on bio-compatible substrates and the enabling technologies for the IoT. He is the Chair of the IEEE Technical Committee MTT-24-RFID Technologies. He is an Associate Editor of *ACES Journal*.

GUENDALINA SIMONCINI (Graduate Student Member, IEEE) received the Laurea degree *(magna cum laude)* in electronics engineering for the IoT from the University of Perugia, Italy, in 2019, where she is currently pursuing the Ph.D. degree in industrial and computer engineering. Her scientific interests include the modeling, design, and characterization of microwave integrated circuits.

VALENTINA PALAZZI (Member, IEEE) received the B.Sc. and M.Sc. degrees *(magna cum laude)* in electronics engineering and the Ph.D. degree in industrial and information engineering from the University of Perugia, Perugia, Italy, in 2012, 2014, and April 2018, respectively. She is currently working as a Researcher with the High Frequency Electronics Laboratory, University of Perugia. In 2015, she was a Visiting Ph.D. Student with the Tyndall National Institute, Cork, Ireland. In 2016, she visited the Centre Tecnològic de Telecomunicacions de Catalunya, Barcelona, Spain, sponsored by the COST Action IC1301 Wireless Power Transmission for Sustainable Electronics. In 2016, she was with the Agile Technologies for High-Performance Electromagnetic Novel Applications Research Group, School of Electrical and Computer Engineering, Georgia Institute of Technology, Atlanta, GA, USA, for five months, where she was involved in additive manufacturing technologies and flexible electronics. Her current research interests include the design of passive transponders with sensing capabilities, radar front ends, wireless power transfer technologies, additive manufacturing processes, and conformal electronics. She is a member of IEEE MTT-S TC-26 RFID, Wireless Sensor, and the IoT. She was a recipient of the First Place Award of the IEEE MTT-S Student Design Competition on Wireless Energy Harvesting from the International Microwave Symposium, in 2016, the IEEE MTT-S Graduate Fellowship, in 2017, the 2017 MTT-S Prize Italy Chapter Central and Southern Italy, and the Young Scientist Best Paper Award, conferred at the 2019 URSI Italian National Meeting.

RAFFAELE SALVATI was born in May 1995. He received the B.Sc. degree in electronics and computer science engineering from the University of Perugia, Italy, in 2017, where he is currently pursuing the M.Sc. degree in electronics engineering for the IoT, working at the master's degree thesis. His scientific interests are related to the design, fabrication, and experimental characterization of electronic circuits for microwave and mm-wave applications.

GIORDANO CICIONI was born in June 1994. He received the B.Sc. degree in electronics and computer science engineering from the University of Perugia, Italy, in 2017, where he is currently pursuing the M.Sc. degree in electronics engineering for the IoT, working at the master's degree thesis. His scientific interests are related to the design, fabrication, and experimental characterization of electronic circuits for microwave and mm-wave applications.

LUCA ROSELLI (Fellow, IEEE) joined the University of Perugia, Perugia, Italy, in 1991. In 2000, he founded the spin-off WiS S.r.l. He was involved in electronic technologies for the Internet of Things for six years. He is currently a Qualified Full Professor with the University of Perugia, where he teaches applied electronics and coordinates the High Frequency Electronics Laboratory. He has authored over 280 articles (h-index 29 with more than 3000 citations, source Google Scholar) and *Green RFID System* (Cambridge University Press, 2014). His current research interests include HF electronic systems with a special attention to RFID, new materials, and wireless power transfer. He was a member of the Board of Directors of ART S.r.l., Urbino, Italy, from 2008 to 2012. He is a member of the list of experts of the Italian Ministry of Research, the past Chair of the IEEE Technical Committees MTT-24-RFID, the Vice Chair of 25-RF Nanotechnologies, 26-Wireless Power Transfer, the ERC Panel PE7, and the Advisory Committee of the IEEE-WPTC, and the Chairman of the SC-32 of IMS. He is the Co-Chair of the IEEE Wireless Sensor Network Conference. He organized the VII Computational Electromagnetic Time Domain, in 2007, and the first IEEE Wireless Power Transfer Conference, in 2013. He is involved on the boards of several international conferences. He is a Reviewer of many international journals, including the Proceedings of the IEEE, the IEEE TRANSACTIONS ON MICROWAVE THEORY AND TECHNIQUES, and the IEEE MICROWAVE AND WIRELESS COMPONENTS LETTERS. He is an Associate Editor of the *IEEE Microwave Magazine*.

FEDERICO DOGO received B.Sc. degree (physics and astronomy) in climatology (greenhouse effect) and the M.Sc. degree (astronomy) in theoretical cosmology (dark energy alternative) from the University of Padua, in 2006 and 2010, respectively, and the Ph.D. degree (physics) in biophysics (ionizing radiation, DNA, and tumors) from the University of Trieste, in 2015. In the University of Padua, he was an assistant curator at the museums of history of physics and mineralogy, from 2006 to 2008. Then, he moved to the University of Trieste. In the same year, he joined PicoSaTs s.r.l., Trieste, Italy, where he is currently focusing on small satellites and CubeSats system design and development.

SIMONE PAULETTO was born in 1997. He received the B.Sc. degree *(magna cum laude)* in electronics and computer science engineering from the University of Trieste, Italy, in 2019. He is currently pursuing the M.Sc. degree in electronics and computer science engineering with the University of Trieste. In the same year, he joined PicoSaTs s.r.l., Trieste, where he is studying electronic systems for small satellites through a research grant. His main area of study is power electronics, specifically switching circuits such as class D power amplifiers and SMPSs.

MARIO FRAGIACOMO was born in October 15, 1940. He received the Diploma degree from the Alessandro Volta Industrial Technical Institute, Trieste, Italy, in 1961, and the Honoris Causa degree in electronics engineering from the University of Trieste, in 1999. From 1961 to 1962, he was employed as a Quality Control Technician at Selenia s.p.A., Rome, Italy, working on the component testing for anti-aircraft missiles. From 1962 to 1965, he was a Designer at Litton Italia s.p.A., Rome, Italy, focusing on professional audio recorders. From 1965 to 1988, he was a Designer, and the Research and Development Director of the IRET s.p.A, Trieste, developing military HF, VHF, and UHF transceivers. From 1988 to 2002, he was the Technical Director of Telit/Telital s.p.A, Trieste. He was also the General Manager Assistant at Telital Research and Development Denmark, Aalborg, Denmark, and the co-founder of the company. Telit/Telital is the only Italian company with comprehensive expertise in the design of the cellular phones (RTMS, TACS, GSM, GLOBALSTAR, UMTS, and now LTE e 5G). From 2001 to 2002, he was a Contract Professor at the Faculty of Engineering, University of Trieste, teaching the class of telecommunication electronics. From 2002 to 2010, he was the Technical Manager of the Enteos s.r.l.–Mywave s.p.A., coordinating the hardware development activities (mobile phones antenna design and RFID sensors). Since 2003, he has been cooperating with the University of Trieste in order to support the activities of students involved in the CubeSat Project. Since 2016, he has been one of the PicoSaTs s.r.l. founders, a spinoff company of the University of Trieste, working on the development of technologies for CubeSats.

ANNA GREGORIO was born in Trieste, Italy, in 1967. She received the Laurea degree *(magna cum laude)* in physics from University of Trieste, Trieste, Italy, in 1992, the master's degree in space systems engineering-Spacetech from Delft University (NL), in 1995, and the Ph.D. degree in physics from the Scuola Normale Superiore, Pisa, Italy, in 2002. Since 1998, she has been a permanent staff at the University of Trieste, Trieste, Italy, as an Associate Professor. Since 2013, her main research project has been related to the Euclid mission of the European Space Agency (ESA), being in charge of coordinating and managing the on-board instruments teams during in-flight operations. Previously, from 1999 to 2013, her main research project was related to the ESA Planck mission, during which she was responsible for on ground testing, in-flight calibration, and the operations of the low frequency instrument (LFI) on board Planck (AIV/AIT manager and instrumental operation team manager). She has participated in ultra-violet spectrograph for astronomical research (UVSTAR), from 1998 to 2003, and on board the Space Shuttle. She is the co-founder and the CEO of PicoSaTs s.r.l., a 2014 University of Trieste spin-off company, focusing on telecommunication systems for small satellites and CubeSats. She has several teaching positions and is currently with the Laboratory of Astrophysics for Space, Space Weather, and Statistics. She has supervised 27 M.Sc. and seven Ph.D. theses. Her h-index is 54 with 306 articles. She has been the University Representative of Consorzio Interuniversitario per la Fisica Spaziale (CIFS) Board of Directors, since 2009, a member of the Scientific Committee of Collegio Fonda, since 2016, and a Reference Person of Tavolo di Consultazione Nazionale H2020–Configurazione Spazio, since 2016. She was a member of University Comitato Unico di Garanzia (CUG), from 2014 to 2018, and a Representative of University in Consorzio Center for Advanced Research in Space Optics (CARSO) Board of Directors, from 2005 to 2008. She is the European Commission expert evaluator (SPACE-20-SCI-2018, EASME, SPACE-30-SCI-2020). She was an invited member of Committee on Space Research (COSPAR) Study Group on Small Satellites for Space Sciences, from 2018 to 2019.